Tailored Phase Transformation of CsPbI₂Br Films by Copper(II) Bromide for High-Performance All-Inorganic Perovskite Solar Cells

Kai-Li Wang,[†,§,∥] Rui Wang,[‡,∥] Zhao-Kui Wang,*[†,‡] Meng Li,[†] Yue Zhang,[†] Heng Ma,[§] Liang-Sheng Liao,*[†] and Yang Yang*[‡]

[†]Institute of Functional Nano and Soft Materials (FUNSOM), Soochow University, Jiangsu Key Laboratory for Carbon-Based Functional Materials and Devices, Suzhou, Jiangsu 215123, China

[‡]Department of Materials Science and Engineering, University of California, Los Angeles, California 90095, United States

[§]College of Physics and Electronic Engineering, Henan Normal University, Xinxiang 453007, P.R. China

S Supporting Information

ABSTRACT: All-inorganic-based perovskites achieved by replacing the organic component with cesium (Cs) have drawn more attention because of their intrinsic inorganic stability. However, the cell efficiency in all-inorganic perovskite solar cells is still far below that in organic−inorganic hybrid perovskite-based devices. Here, we develop a new strategy to mediate the CsPbI₂Br crystallization by directly doping copper(II) bromide (CuBr₂) into a perovskite precursor. The incorporation of CuBr₂ played a role in retarding the crystallization dynamics process of CsPbI₂Br film, resulting in a high-quality all-inorganic perovskite film with enlarged grain size, improved carrier mobilities, and reduced trap states. The fabricated perovskite solar cells delivered a champion power conversion efficiency of 16.15%, which is the highest efficiency in CsPbI₂Br based all-inorganic perovskite solar cells and largely higher than 13.24% for pristine CsPbI₂Br based device. The developed doping method paves a new route to fabricate high-performance all-inorganic perovskite solar cells.

KEYWORDS: Inorganic perovskites, CsPbI₂Br, phase transformation, crystallization, copper(II) bromide
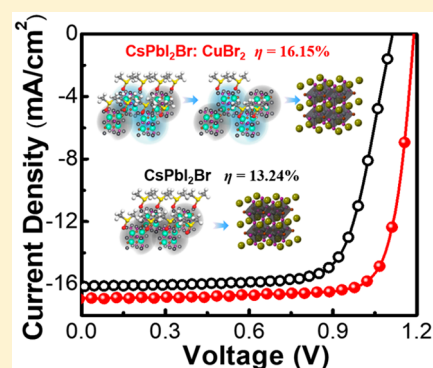
Organic−inorganic hybrid perovskites are regarded as promising next-generation photovoltaic materials because of their excellent semiconducting properties such as suitable band gap, high carrier mobility, and long charge diffusion length. With these merits, the power conversion efficiency (PCE) of organic−inorganic hybrid perovskite solar cells (PSCs) has skyrocketed from 3.8% to 23.3% within the past decade.[1,2] However, the organic parts such as methylammonium (MA) and formamidinium (FA) make the hybrid perovskite materials suffer from poor thermal, optical, and moist stabilities.[3−5] Although the instability issue could be partially addressed by substitution,[6−8] cation-exchange,[9,10] additives,[11−13] and encapsulation,[14,15] the intrinsic instability of organic−inorganic hybrid perovskite materials is still a serious challenge for commercial application of PSCs. Recently, all-inorganic-based perovskites by replacing the organic component with cesium (Cs) have drawn much attention owing to their intrinsic stability.[16−18]

For example, the inorganic perovskite CsPbX₃ (X= Cl, Br, I) is reported to exhibit better thermal stability than the organic−inorganic-based one.[16,18] Particularly, CsPbI₃ in the cubic phase (α-phase) possesses an appropriate optical energy band gap (Eg) of 1.73 eV,[19] which is beneficial to configure a tandem device by combining it with other low band gap solar cells.[20−24] Recently, several groups have reported CsPbI₃-

based PSCs with PCE exceeding 15%.[25,26] Unfortunately, CsPbI₃ film suffers from serious phase instability because α-CsPbI₃ is just stable over 330 °C and prone to be converted into a nonperovskite phase (δ-CsPbI₃) at room temperature.[27] In contrast, CsPbBr₃ has a stable orthorhombic phase at room temperature. It can be easily transformed into high-symmetry tetragonal and cubic phase by annealing at 88 and 130 °C, respectively.[28] However, the larger bandgap (∼2.3 eV) restricts its absorption in the visible light region. This causes low short-circuit current density (Jsc) and thus low PCE in single-junction cells.[29] Alternatively, mixed-halide inorganic perovskites, CsPbI₃₋ₓBrₓ, are feasible materials to possess low phase transition temperature and tunable band gap by a I/Br composition engineering.[30−34] For example, Lau et al. reported a PCE of 6.3% in all-inorganic PSCs based on CsPbIBr₂ with an Eg of 2.05 eV.[32] Zeng et al. developed a polymer-passivated CsPbI₂Br film with an Eg of 1.82 eV, giving an PCE over 12% in corresponding PSCs with a large Voc up to 1.32 V.[33] Liu et al. designed inorganic PSCs based on 3D-2D-0D CsPbI₂Br multiple graded heterojunction with a PCE of 12.39%.[34] These promising achievements indicate that the mixed-halide
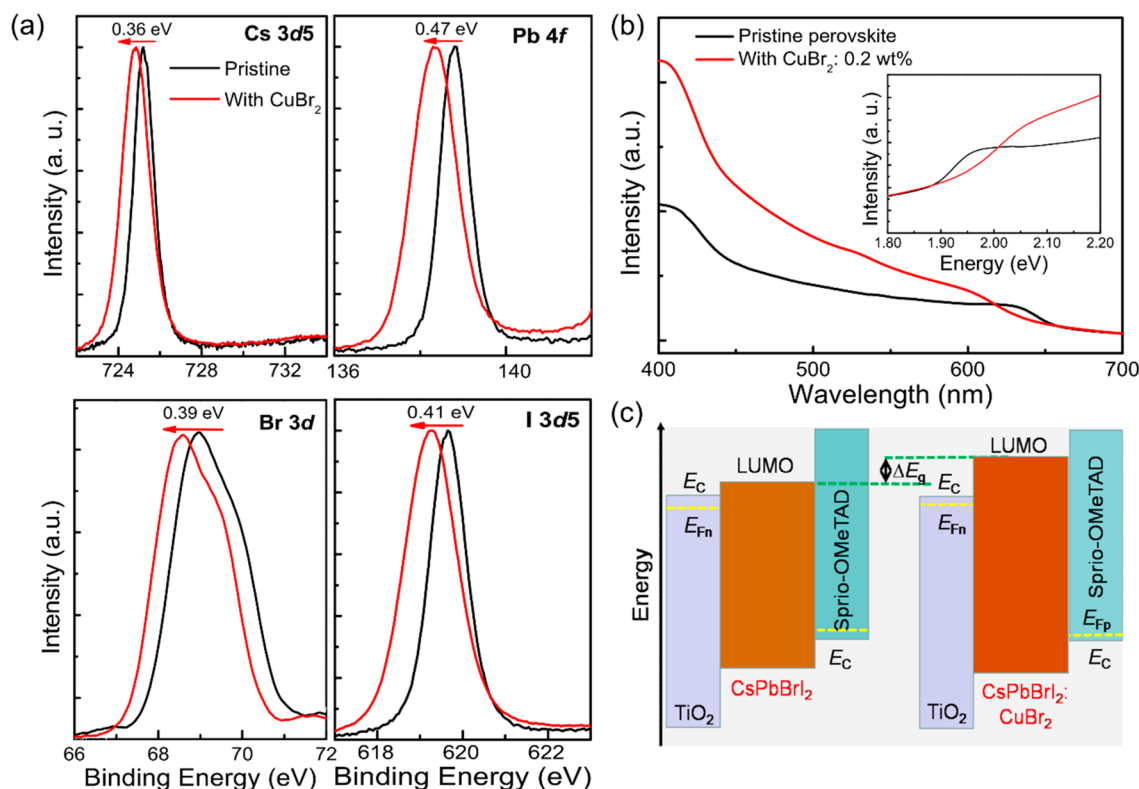
Figure 1. (a) XPS spectra for Cs 3d5, Pb 4f, Br 3d, and I 3d5 in CsPbI$_2$Br and CsPbI$_2$Br/CuBr$_2$ (0.2 wt %) perovskite films. (b) UV−vis spectra of CsPbI$_2$Br and CsPbI$_2$Br/CuBr$_2$ (0.2 wt %) perovskite films. (c) Schematic energy level diagram of CsPbI$_2$Br and CsPbI$_2$Br/CuBr$_2$ based perovskite solar cells.

inorganic perovskites have great potential in realizing highly efficient and long-term stable all-inorganic PSCs.

High-quality polycrystalline all-inorganic perovskite films with good morphology and large grain size are desirable for realizing high-performance devices. Unfortunately, defects and traps are inevitable in most solution-processed perovskite films.[35,36] Similar with the organic−inorganic hybrid perovskites,[37−42] various methods for trap passivation among grain boundaries and/or on surfaces, such as partial substitution and/or incorporation of metal cations anions, have been developed in mixed-halide inorganic PSCs.[43−47] However, the cell efficiency in mixed-halide inorganic PSCs is still far below that of organic−inorganic hybrid-based ones. Therefore, further strategies of reducing the defects and traps in mixed-halide inorganic perovskite films are necessary. Herein, we reported a facial passivation route for CsPbI$_2$Br films by a direct incorporation of copper bromide (CuBr$_2$) into perovskite precursor. Bromine salt is selected to avoid additional incorporation of impurities into the perovskite films. CuBr$_2$ incorporation plays an important role in improving the CsPbI$_2$Br crystallization with large grain size and full film coverage by retarding the crystalline dynamic process. As a result, the fabricated all-inorganic perovskite solar cells employing CsPbI$_2$Br/CuBr$_2$ as the absorber layer exhibit a maximum PCE of 16.15% with a V_{oc} of 1.18 V, a J_{sc} of 16.95 mA cm^{-2}, and a FF of 0.80.

CuBr$_2$-Doped CsPbI$_2$Br Films. CsPbI$_2$Br precursor solution was prepared by dissolving CsI/CsBr/PbI$_2$/PbBr$_2$ (1:0.5:1:0.5) in dimethyl sulfoxide (DMSO) with a 0.8 M concentration. CsPbI$_2$Br/CuBr$_2$ composite perovskite films were deposited in a N$_2$ glovebox by spin-coating CuBr$_2$-incorporated CsPbI$_2$Br precursor onto compact TiO$_2$ layer

with desired doping ratios. The samples were treated with chlorobenzene drop-casting during spin-coating and subsequently annealed at 260 °C for 10 min.

To clarify the effect of CuBr$_2$ incorporation on the electrical structure and chemical states of CsPbI$_2$Br, X-ray photoelectron spectra (XPS) of corresponding pristine and composite perovskite films are evaluated. Figure 1a plots the XPS results of Cs 3d5, Pb 4f, Br 3d, and I 3d5 core levels in pristine CsPbI$_2$Br and CsPbI$_2$Br/CuBr$_2$ (0.2 wt %) films. Compared to the pristine CsPbI$_2$Br film, the core level peaks of all four elements in CsPbI$_2$Br/CuBr$_2$ composite film are seen slightly blue-shifted by 0.36, 0.47, 0.39 and 0.41 eV for Cs 3d5, Pb 4f, Br 3d, and I 3d5, respectively. We ascribe these shifts to the doping of CsPbI$_2$Br by CuBr$_2$ because simple blending would not cause a large change of chemical state.[44,48] To further inspect the electronic structure of the CsPbI$_2$Br/CuBr$_2$ (0.2 wt %) perovskite, the perovsite film was scraped off and the obtained power was put onto a copper grid for evaluation. The selected area electron diffraction (SAED) patterns of CsPbI$_2$Br and CsPbI$_2$Br/CuBr$_2$ (0.2 wt %) perovskites are shown in Figure S1a,b, respectively. It is found that both samples are composed of some single crystals due to their distinct electron diffraction patterns. Figure S1c,d shows the high-resolution transmission electron microscope (HRTEM) images of dispersed CsPbI$_2$Br and CsPbI$_2$Br/CuBr$_2$ (0.2 wt %) perovskite scraped from their films. The lattice parameter of CsPbI$_2$Br films was determined to be 0.31 nm, matching well the spacing of (100) crystal planes in the cubic CsPbBrI$_2$ crystal structure.[49] In contrast, CsPbI$_2$Br/CuBr$_2$ (0.2 wt %) sample has a slightly decreased lattice parameter of 0.30 nm, which is correlative with the lattice distortion caused by the smaller atomic radius of Cu compared with Pb. Meanwhile, the
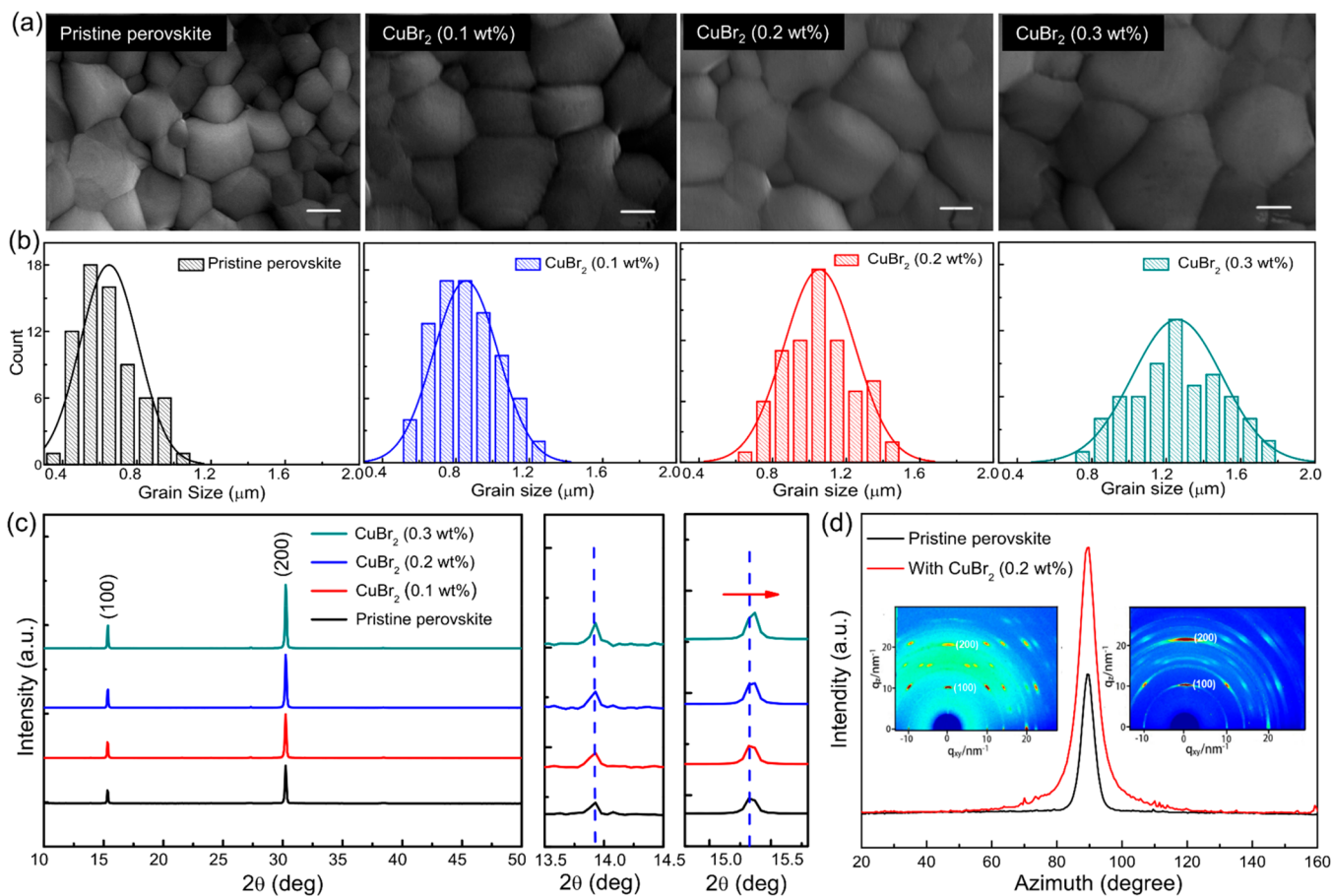
Figure 2. (a) Top-view SEM images (scale bar, 400 nm) and (b) grain size statistical distribution of CsPbI$_2$Br films with various CuBr$_2$ ratio (0, 0.1, 0.2, and 0.3 wt %). (c) XRD profiles of corresponding CsPbI$_2$Br/CuBr$_2$ perovskite films. (d) Radially integrated intensity plots along the ring assigned to the (100) planes of CsPbI$_2$Br and CsPbI$_2$Br/ CuBr$_2$ (0.2 wt %) films. Insets are the corresponding GIXRD patterns.

imperceptible change in lattice parameter resulted from insufficient CuBr$_2$ doping.

A comparison of photophysical properties of pristine CsPbI$_2$Br and composite CsPbI$_2$Br/CuBr$_2$ films was further investigated. Figure 1b presents the absorbance spectra of CsPbI$_2$Br and CsPbI$_2$Br/CuBr$_2$ (0.2 wt %) films. The CsPbI$_2$Br/CuBr$_2$ film showed obviously enhanced optical absorption in the whole region beyond 630 nm compared to the pristine perovskite film. The Tauc plot shown in the inset of Figure 1b indicated that the band gap of CsPbI$_2$Br was increased from 1.88 to 1.95 eV after doping with 0.2 wt % CuBr$_2$. To further clarify the doping effect of CuBr$_2$ on the electronic structure of CsPbI$_2$Br, density functional theory (DFT) calculations based on the exchange-correlation functions of generalized gradient approximation (GGA) with Perdew−Burke−Ernzerhof (PBE) were executed. The calculation was carried out based on CsPbI$_2$Br orthorhombic phase with space group of *Pnma*. One Cu atom substitutes one Pb atom from 16 equiv sites as shown in Supporting Information Figure S2. The simulation results give a similar trend of increased band gap in CsPbI$_2$Br by CuBr$_2$ doping. Interestingly, this phenomenon is different from the case of organic−inorganic hybrid perovskite in which Cu^{2+} doping reduced the band gap of CH$_3$NH$_3$PbI$_3$.[50] In planar structure PSCs, the band gap of perovskite absorber layer and the energy levels of interfacial layers are the main factors to determine the V_{oc} of the devices. Figure 1c presents a schematic of the energy levels of used materials in pristine CsPbI$_2$Br and CsPbI$_2$Br/CuBr$_2$

based PSCs. Obviously, the V_{oc} is expected to be increased owing to the enlarged E_g by CuBr$_2$ doping.

The effects of CuBr$_2$ doping on the crystalline and morphological properties of CsPbI$_2$Br films were further evaluated. Figure 2a shows the top-view scanning electron microscopy (SEM) images of CsPbI$_2$Br/CuBr$_2$ films with varied doping ratios (0−0.3 wt %). Compared to pristine CsPbI$_2$Br film, the grain size in CsPbI$_2$Br/CuBr$_2$ films is enlarged with CuBr$_2$ doping ratio. The statistical distribution of the grain size in each film is ploted in Figure 2b. The average grain size in pristine CsPbI$_2$Br, CsPbI$_2$Br/CuBr$_2$ (0.1 wt %), CsPbI$_2$Br/CuBr$_2$ (0.2 wt %), and CsPbI$_2$Br/CuBr$_2$ (0.3 wt %) films was 643, 848, 1051, and 1255 nm, respectively. Although the grain size was enlarged, the CuBr$_2$ doping did not deteriorate the film morphology largely (Supporting Information, Figure S3).

Figure 2c shows the X-ray diffraction (XRD) patterns of corresponding CsPbI$_2$Br/CuBr$_2$ films. All samples exhibited a typical perovskite after a high-temperature annealing process at 260 °C. The main diffraction peaks at 15.37° and 30.18° were assigned to (100) and (200) planes of CsPbI$_2$Br δ-phase.[32] Obviously, the diffraction peak intensities in CsPbI$_2$Br/CuBr$_2$ films were stronger than that in pristine CsPbI$_2$Br film, indicating an improved crystalline quality by CuBr$_2$ doping. The diffraction peak of PbI$_2$ was clearly observed in the magnified illustration shown in the right of Figure 2c. Furthermore, the intensity of PbI$_2$ was increased with the CuBr$_2$ doping ratio. According to previous studies,[51,52] the
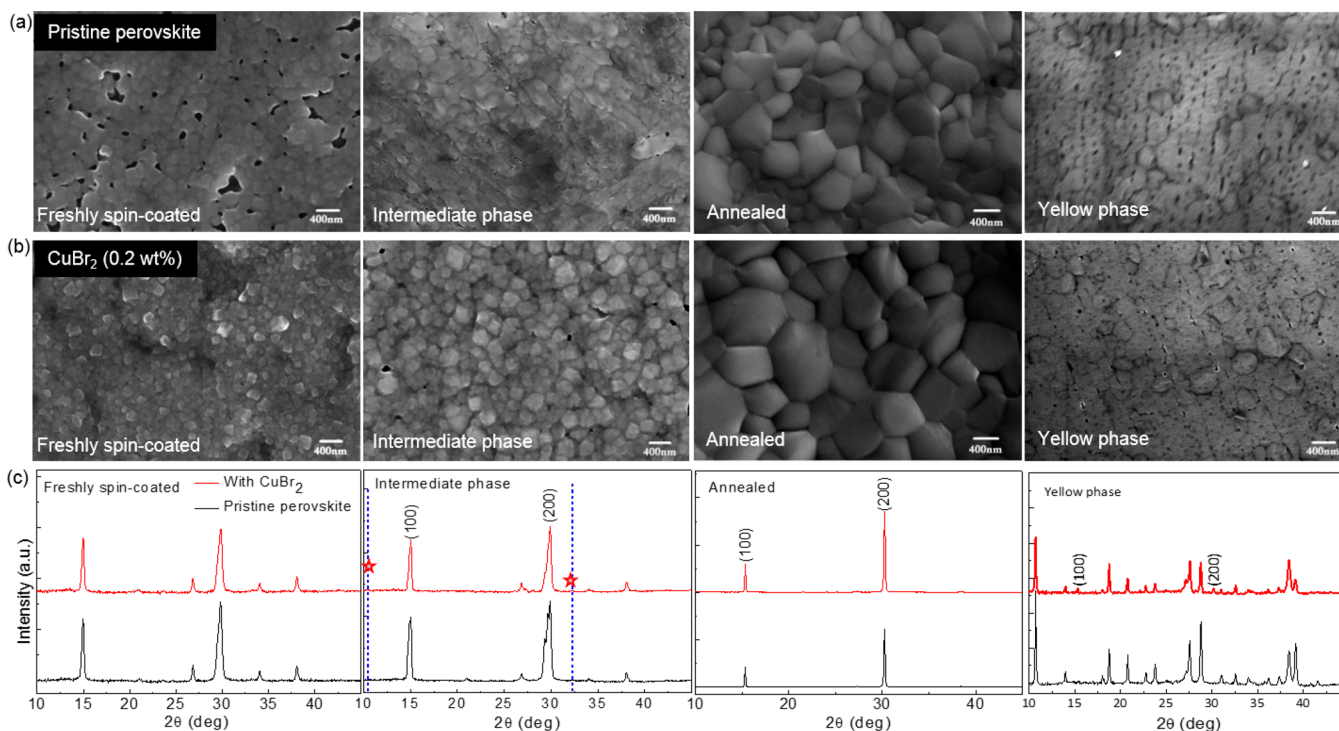
Figure 3. Top SEM images of (a) CsPbI$_2$Br and (b) CsPbI$_2$Br/CuBr$_2$ (0.2 wt %) films at typical steps during perovskite formation. (c) XRD patterns of CsPbI$_2$Br and CsPbI$_2$Br/CuBr$_2$ (0.2 wt %) films at corresponding steps.

appropriate amount of PbI$_2$ could effectively passivate the perovskite film with reduced defects and traps, whereas excessive PbI$_2$ would lower the crystalline quality of perovskite films. In addition, (100) peak was shifted to a higher degree, indicating an incorporation of smaller Cu atoms into the lattice sites of CsPbI$_2$Br.[53,54] The high crystalline quality of CsPbI$_2$Br/CuBr$_2$ film was further revealed by grazing incidence X-ray diffraction (GIXRD) measurements. The inset of Figure 2d plots the 2D GIXRD profiles of pristine CsPbI$_2$Br and CsPbI$_2$Br/CuBr$_2$ (0.2 wt %) films. Compared to the pristine film, the appearance of strongly scattered secondary spots and rings in CsPbI$_2$Br/CuBr$_2$ film suggests that the polycrystalline film was grown with good orientation relative to the substrate plane. The preferred orientation in the CsPbI$_2$Br/CuBr$_2$ film was further proven by the plots of azimuthally integrated scattering intensities for two samples as shown in Figure 2d. Obviously, the peak intensity at 90° azimuth in CsPbI$_2$Br/CuBr$_2$ film was higher than that in pristine CsPbI$_2$Br perovskite film, indicating a highly ordered orientation along (100) plane.[55−59] The preferred crystalline orientation means less defects and traps, which would improve the charge transport along the preferred direction and reduce the carrier recombination.

Furthermore, combined evaluation of SEM and XRD on typical steps during the formation of perovskite films is carried out to investigate the role of CuBr$_2$ in assisting the crystallization dynamics process of CsPbI$_2$Br. As shown in Figure 3, the freshly spin-coated CsPbI$_2$Br/CuBr$_2$ film presented poor crystalline quality with smaller grain size compared with pristine CsPbI$_2$Br film. At a yellow phase before annealing, two new peaks at 12° and 32° were observed in both samples, indicating that the samples possess an intermediate phase. Noticeably, CsPbI$_2$Br/CuBr$_2$ film showed improved crystallization with larger grain size. However, more

pinholes and voids were observed. After annealing, both films demonstrated compact morphology with excellent crystallization. Similar with Figure 2, CsPbI$_2$Br/CuBr$_2$ film exhibited superior crystallization with larger grain size compared with pristine CsPbI$_2$Br film. The growing of perovskite film from initial small grain size to final large grain size suggests a slower crystallization dynamics process in CsPbI$_2$Br/CuBr$_2$ film. It means that CuBr$_2$ played an important role in retarding the crystallization rate of the CsPbI$_2$Br film. The direct comparison of photographs between the colors of CsPbI$_2$Br and CsPbI$_2$Br/CuBr$_2$ films further revealed the slow crystallization process in CuBr$_2$-doped CsPbI$_2$Br film (Supporting Information, Figure S4). To further understand the effect of CuBr$_2$ doping on the stability of perovskite phase, Figure 3 shows the XRD patterns of perovskite films with or without CuBr$_2$ doping after exposure to ambient for more than 24 h. Exposure to ambient restores the films to the yellow phase. Nevertheless, CsPbI$_2$Br/CuBr$_2$ film still kept part δ-phase with weak intensities of (100) and (200) peaks, indicating improved stability in CsPbI$_2$Br by CuBr$_2$ doping.

Photovoltaic Performance. To investigate the effect of CuBr$_2$ doping on photovoltaic performance, n-i-p PSCs with a structure of FTO/TiO$_2$/CsPbI$_2$Br/CuBr$_2$/Spiro-OMeTAD/MoO$_3$/Ag were fabricated (the area of device is 0.09 cm^2). Figure 4a shows the CuBr$_2$ ratio dependent J−V characteristics of CsPbI$_2$Br/CuBr$_2$ based PSCs under the AM 1.5G illumination with the light intensity of 100 mW cm^{-2}. The main cell parameters are summarized in Table 1. The reference device without CuBr$_2$ doping presented a PCE of 13.24%, a short-circuit current density (J_{sc}) of 16.18 mA cm^{-2}, a V_{oc} of 1.12 V, and a fill factor (FF) of 0.73. The positive effect of CuBr$_2$ incorporation was very obvious even at a very small amount. By doping 0.1 wt % CuBr$_2$, V_{oc} and J_{sc} were increased to 1.16 V and 16.92 mA cm^{-2}, respectively. At an optimized
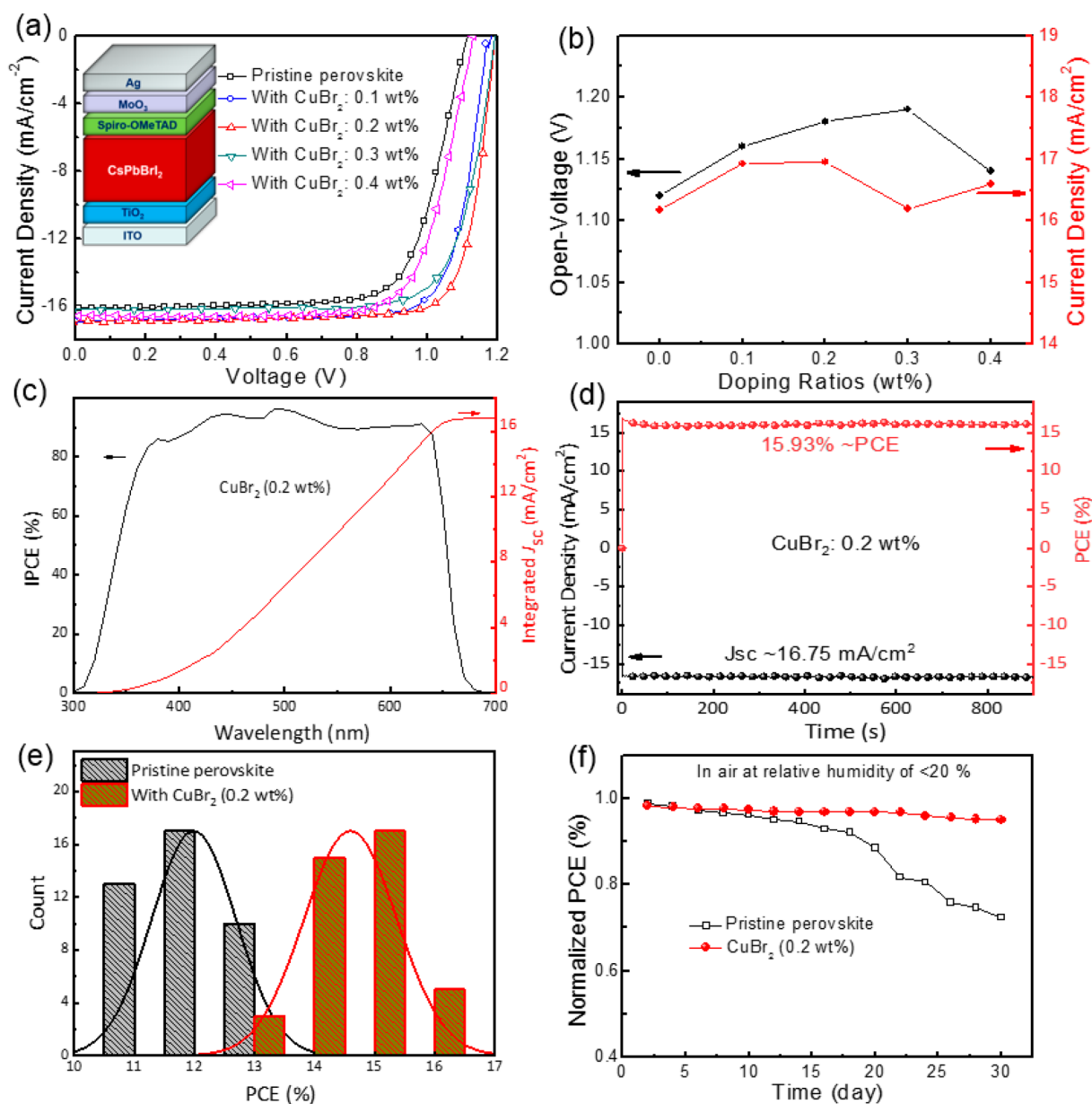
Figure 4. (a) $J-V$ curves of perovskite solar cells measured under simulated AM 1.5 sunlight of 100 mW cm^{-2}. (b) Doping ratio dependence of open voltage and current density in devices with CsPbI$_2$Br and CsPbI$_2$Br/CuBr$_2$ (0.2 wt %) films. (c) IPCE spectra and (d) steady power output curves for CsPbI$_2$Br/CuBr$_2$ (0.2 wt %) based device and their corresponding photocurrent output at 0.87 V. (e) A histogram of PCEs measured from CsPbI$_2$Br and CsPbI$_2$Br/CuBr$_2$ (0.2 wt %) based device. (f) Long-term stability of CsPbI$_2$Br/CuBr$_2$ (0.2 wt %) based devices without encapsulation.

Table 1. Cell Parameters of CsPbI$_2$Br/CuBr$_2$ based Perovskite Solar Cells with Various CuBr$_2$ Doping Ratio

perovskites	V_{oc} (V)	J_{sc} (mA/cm^2)	FF	PCE (%)
pristine perovskite	1.12	16.18	0.73	13.24
with CuBr$_2$: 0.1 wt %	1.16	16.92	0.79	15.45
with CuBr$_2$: 0.2 wt %	1.18	16.95	0.80	16.15
with CuBr$_2$: 0.3 wt %	1.19	16.20	0.77	14.89
with CuBr$_2$: 0.4 wt %	1.14	16.59	0.74	13.99

doping ratio of 0.2 wt %, the device approached a maximum PCE of 16.15% with a V_{oc} of 1.18 V, a J_{sc} of 16.95 mA cm^{-2}, and an FF of 0.80. In addition, the cell was aged for 150 h under continuous illumination with full intensity and maximum power point tracking (MPPT) in a nitrogen

atmosphere (Figure S5), and the device retained more than 80% of its initial performance. Figure 4b plots the changes of V_{oc} and J_{sc} with CuBr$_2$ doping ratio. J_{sc} achieved the maximum at the optimized doping ratio of 0.2 wt %. However, V_{oc} reached a maximum of 1.19 V when the doping ratio was further increased to 0.3 wt %. The incident-photon-to-current efficiency (IPCE) spectra of the reference device and the champion device are displayed in Figure 4c. In the absorbance range from 420 to 640 nm, almost all of EQE values are exceeding 85%. From IPCE values, the integrated current density is 16.78 mA cm^{-2}, which agrees well with the value from $J-V$ curve. Figure 4d gives the steady-state photocurrent and PCE values measured over a period of 900 s at the maximum power point of 0.87 V, and these devices are very

stable with the PCE of 15.93% for over 900 s in ambient. To verify the reproducibility of high efficiency, 40 individual $CsPbI_2Br/CuBr_2$ based devices were fabricated. The histograms of PCE distributions are plotted in Figure 4e. The PCE distribution exhibits a small deviation with an average value of 14.6%, indicating a better device reproducibility.

Besides the device efficiency, the cell stability is another critical concern for perovskite solar cells. The device reliabilities of $CsPbI_2Br$ and $CsPbI_2Br/CuBr_2$ based PSCs were evaluated without encapsulation in ambient at room temperature and <20% relative humidity. Figure 4f shows PCE decay as a function of time for one month. The reference device presents a poor stability during the test. The PCE reduces to 92% of the initial value after 18 days' aging. After that, the degradation rate increased with a rapid drop in PCE. It further deteriorated to 73% after 30 days continuous degradation. In contrast, $CsPbI_2Br/CuBr_2$ based device exhibits an excellent stability by remaining 95% of the initial value after one month aging. This means that the incorporation of $CuBr_2$ could play a very positive role in improving the cell stability of $CsPbI_2Br$ based all-inorganic PSC.

To clarify the positive influence of $CuBr_2$ on the cell performance, a detailed investigation on the elements distributions and carrier dynamic process in the device was executed. Figure 5a,b gives the time-of-flight secondary ion mass spectroscopy (TOF-SIMS) depth profiles including CN, Ag, Pb, Cs, and Cu elements in $CsPbI_2Br$ and $CsPbI_2Br/CuBr_2$ based PSCs. The insets show the 3D distribution for these elements. As expected, Cu elements are distributed homogeneously throughout the perovskite film similar to Pb and Cs elements. The energy-dispersive X-ray spectroscopy (EDS) mapping of Cu and Br elements further verifies the uniform distribution of $CuBr_2$ in $CsPbI_2Br/CuBr_2$ film (Supporting Information, Figure S6). In addition, there was no evident shift of the TOF-SIMS depth profiles of Pb and Cs elements in two devices, suggesting that the incorporation of $CuBr_2$ did not change the distribution of other elements. To explore the degradation origin of $CsPbI_2Br/CuBr_2$ film during a long-time operation, TOF-SIMS was performed to detect changes to the chemical composition in a sample of $FTO/TiO_2/CsPbI_2Br/CuBr_2$. The sample was kept at ambient temperature with 60% humidity for over 24 h until it completely transformed into a yellow phase. As shown in Supporting Information Figure S7, there is no obvious diffusion of the Cu element as the sample transforms into a yellow phase on aging. The depth profiles of TOF-SIMS provided the direct information on key elemental distributions in the device before and after degradation.

The diode behavior was evaluated by getting rid of the other possible interference induced by light, and typical dark $J−V$ characteristics in $CsPbI_2Br$ and $CsPbI_2Br/CuBr_2$ PSCs are shown in Figure 6a. Compared to the reference device, the

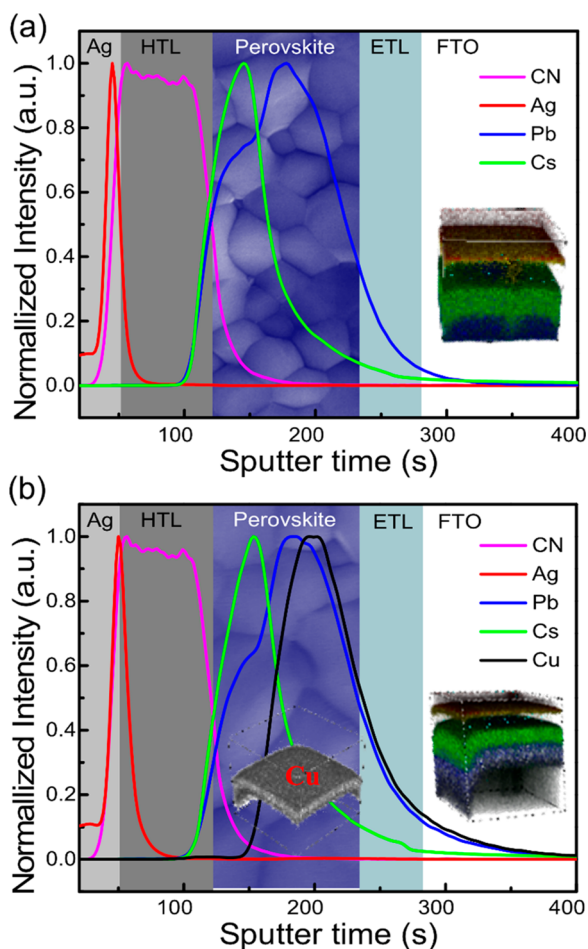**Figure 5.** Time-of-flight secondary ion mass spectroscopy (TOF-SIMS) depth profiles of (a) $CsPbI_2Br$ and (b) $CsPbI_2Br/CuBr_2$ (0.2 wt %) based perovskite solar cells.
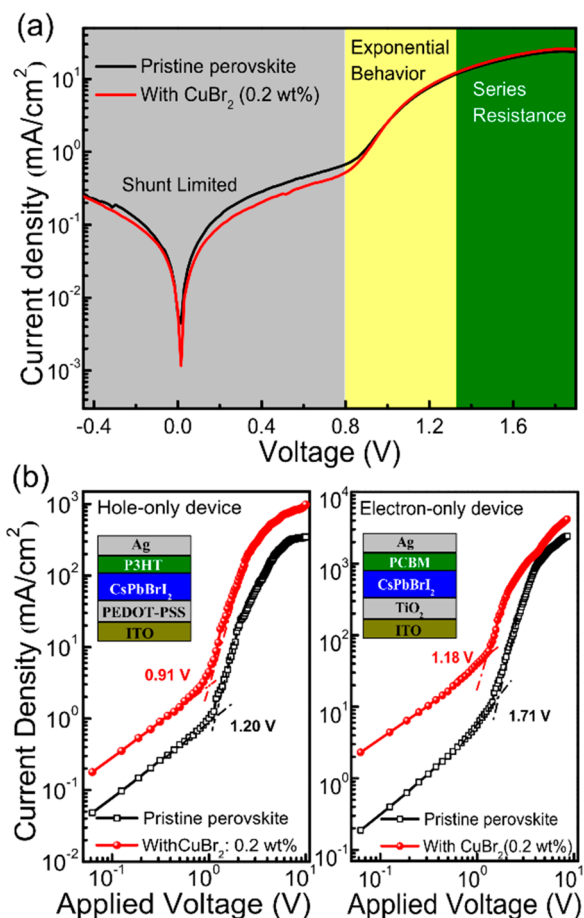

Figure 6. (a) Dark $J−V$ curves in $CsPbI_2Br$ and $CsPbI_2Br$: $CuBr_2$ (0.2 wt %) based perovskite solar cells. (b) Dark $J−V$ characteristics of hole-only and electron-only devices with or without $CuBr_2$ (0.2 wt %) doping.

Table 2. Electronic Properties of CsPbI$_2$Br and CsPbI$_2$Br/CuBr$_2$ (0.2 wt %) Based Perovskite Solar Cells

device	τ_{ave} (ns)	τ_{t-e} (cm^{-3})	τ_{t-h} (cm^{-3})	u_e (cm^2 V^{-1} s^{-1})	u_h (cm^2 V^{-1} s^{-1})
pristine perovskite	14.93	8.60×10^{16}	8.60×10^{16}	0.23	0.92
with CuBr$_2$: 0.2 wt %	3.16	5.90×10^{16}	4.55×10^{16}	0.99	1.55

CuBr$_2$-doped device exhibited lower leakage current. In the exponential behavior regime, the ideal factor n can be derived from[60]

$$\ln(J) = \ln(J_0) + \left(\frac{1}{n}\right)\frac{q}{k_B T}V \qquad (1)$$

where J is the current density, J_0 is the reverse saturation current density, q is the elemental charge, k_B is the Boltzmann constant, and T is the temperature. By fitting the dark $J-V$ curve, the ideal factor n is extrapolated to be 3.4 and 2.5 for CsPbI$_2$Br and CsPbI$_2$Br/CuBr$_2$ based devices, respectively. The large decrease of ideal factor indicates that the incorporation of CuBr$_2$ could enable the device to deliver a better diode junction quality.[60] The electron extraction dynamics process in CsPbI$_2$Br and CsPbI$_2$Br/CuBr$_2$ films were further investigated by steady-state photoluminescence (PL) and time-resolved photoluminescence (TRPL) spectra (Supporting Information, Figure S8). CsPbI$_2$Br/CuBr$_2$ film demonstrated stronger PL quenching than the pristine CsPbI$_2$Br film. The blue shift of PL emission peak and the decreased Stokes shift in the CsPbI$_2$Br/CuBr$_2$ film suggests the positive role of CuBr$_2$ incorporation.[61,62] The shortened PL lifetime from 14.93 to 3.16 ns further confirmed the fast charge extraction in CsPbI$_2$Br/CuBr$_2$ film compared with the pristine CsPbI$_2$Br film. We ascribe it to an excellent grain boundary passivation by CuBr$_2$ with reduced defect states.

To compare the trap states in CsPbI$_2$Br and CsPbI$_2$Br/CuBr$_2$ based devices, the charge transport characteristics in two devices were evaluated. Figure 6b shows the $J-V$ curves by double-logarithmic plots of CsPbI$_2$Br- and CsPbI$_2$Br/CuBr$_2$ based hole-only and electron-only devices. Typical $J-V$ shapes with three regions, Ohmic current, trap-fill limited (TFL) current and space charge limited current (SCLC),[63−66] were observed in four devices. The trap densities (n) could be calculated by $n = (2V_{TFL}\varepsilon\varepsilon_0)/eL^2$, where V_{TFL} is the trap-fill limit voltage, L is the thickness of CsPbI$_2$Br active layer, ε is the relative dielectric constant of CsPbI$_2$Br, ε_0 is the vacuum permittivity, and e is the electron charge. As shown in Table 2, CuBr$_2$-doped CsPbI$_2$Br films show significantly reduced trap density regardless of hole-only or electron-only devices. The hole and electron mobilities were further calculated according to Mott−Gurney's equation $\mu = (8JL^3)/(9\varepsilon\varepsilon_0 V^2)$[67−69] in the SCLC region. By CuBr$_2$ doping, the hole and electron mobilities were increased from 0.92 to 1.55 cm^2 V^{-1} S^{-1} and from 0.23 to 0.99 cm^2 V^{-1} S^{-1}, respectively. The reduced trap states and improved carrier mobilities were attributed to the improved crystal quality of CsPbI$_2$Br films by CuBr$_2$ doping. We see this as the main reason for the largely improved device performance in CsPbI$_2$Br/CuBr$_2$ based devices.

In conclusion, we have demonstrated a high-performance all-inorganic perovskite solar cell by using CuBr$_2$-mediated CsPbI$_2$Br film as the absorber layer. CuBr$_2$ is directly incorporated into the CsPbI$_2$Br precursor by controlling the perovskite crystallization with suppressed nucleation rate during the annealing process. The retarded crystalline dynamics process results in a high quality all-inorganic perovskite film with enlarged grain size, improved carrier mobilities and reduced trap states. Accordingly, the cell efficiency is largely increased from 13.24% to 16.15% owing to simultaneous enhancements in the cell parameters of V_{oc}, J_{sc}, and FF. In addition, the resulting devices also present an excellent stability by retaining 95% of the initial value after one month's aging. This simple strategy opens a new route to realizing highly efficient and stable all-inorganic perovskite solar cells.

■ ASSOCIATED CONTENT

ⓈSupporting Information

The Supporting Information is available free of charge on the ACS Publications website at DOI: 10.1021/acs.nanolett.9b01553.

    Experimental section and additional figures (PDF)

■ AUTHOR INFORMATION

Corresponding Authors
*(Z.K.W) E-mail: zkwang@suda.edu.cn.
*(L.S.L) E-mail: lsliao@suda.edu.cn.
*(Y.Y.) E-mail: yangy@ucla.edu.

ORCID ⓘ
Zhao-Kui Wang: 0000-0003-1707-499X
Liang-Sheng Liao: 0000-0002-2352-9666
Yang Yang: 0000-0001-8833-7641

Author Contributions
‖K.L.W. and R.W. contributed equally to this work.

Notes
The authors declare no competing financial interest.

■ ACKNOWLEDGMENTS

■ REFERENCES

(1) Kojima, A.; Teshima, K.; Shirai, Y.; Miyasaka, T. *J. Am. Chem. Soc.* **2009**, *131*, 6050−6051.
(2) Jeon, N. J.; Na, H.; Jung, E. H.; Yang, T.-Y.; Lee, Y. G.; Kim, G.; Shin, H.-W.; Seok, S. I.; Lee, J.; Seo, Jeon N J.; Na, H.; Jung, E. H.; et al. *Nat. Energy* **2018**, *3*, 682.
(3) Song, T.-B.; Yokoyama, T.; Stoumpos, C. C.; Logsdon, J.; Cao, D. H.; Wasielewski, M. R.; et al. *J. Am. Chem. Soc.* **2017**, *139*, 836−842.
(4) Yang, Y.; You, J. *Nature* **2017**, *544*, 155.

(5) Tsai, H.; Nie, W.; Blancon, J.-C.; Stoumpos, C. C.; Asadpour, R.; Harutyunyan, B.; Neukirch, A. J.; Verduzco, R.; Crochet, J. J.; Tretiak, S.; et al. *Nature* **2016**, *536*, 312.

(6) Li, W.; Zhang, C.; Ma, Y.; Liu, C.; Fan, J.; Mai, Y.; Schropp, R. E. *Energy Environ. Sci.* **2018**, *11*, 286−293.

(7) Wang, Z. K.; Li, M.; Yang, Y. G.; Hu, Y.; Ma, H.; Gao, X. Y.; Liao, L. S. *Adv. Mater.* **2016**, *28*, 6695−6703.

(8) Li, M.; Wang, Z. K.; Zhuo, M. P.; Hu, Y.; Hu, K. H.; Ye, Q. Q.; Jain, S. M.; Yang, Y. G.; Gao, X. Y.; Liao, L. S. *Adv. Mater.* **2018**, *30*, 1800258.

(9) Zhang, H.; Wang, H.; Williams, S. T.; Xiong, D.; Zhang, W.; Chueh, C. C.; Chen, W.; Jen, A. K. Y. *Adv. Mater.* **2017**, *29*, 1606608.

(10) Chen, Q.; Chen, L.; Ye, F.; Zhao, T.; Tang, F.; Rajagopal, A.; Jiang, Z.; Jiang, S.; Jen, A. K.-Y.; Xie, Y.; et al. *Nano Lett.* **2017**, *17*, 3231−3237.

(11) Gong, X.; Li, M.; Shi, X. B.; Ma, H.; Wang, Z. K.; Liao, L. S. *Adv. Funct. Mater.* **2015**, *25*, 6671−6678.

(12) Liu, C.; Li, W.; Zhang, C.; Ma, Y.; Fan, J.; Mai, Y. *J. Am. Chem. Soc.* **2018**, *140*, 3825−3828.

(13) Yang, Z.; Chueh, C. C.; Zuo, F.; Kim, J. H.; Liang, P. W.; Jen, A. K. Y. *Adv. Energy Mater.* **2015**, *5*, 1500328.

(14) Huang, J.; Tan, S.; Lund, P. D.; Zhou, H. *Energy Environ. Sci.* **2017**, *10*, 2284−2311.

(15) Chen, S.; Duan, J.; Tang, Y.; Jin, B.; Qiao, S. Z.; et al. *Nano Energy* **2015**, *11*, 11−18.

(16) Wang, Q.; Dong, Q.; Li, T.; Gruverman, A.; Huang, J. *Adv. Mater.* **2016**, *28*, 6734−6739.

(17) Liu, C.; Li, W.; Zhang, C.; Ma, Y.; Fan, J.; Mai, Y. *J. Am. Chem. Soc.* **2018**, *140*, 3825−3828.

(18) Kulbak, M.; Cahen, D.; Hodes, G. *J. Phys. Chem. Lett.* **2015**, *6*, 2452−2456.

(19) Liang, J.; Wang, C.; Wang, Y.; Xu, Z.; Lu, Z.; Ma, Y.; Zhu, H.; Hu, Y.; Xiao, C.; Yi, X.; et al. *J. Am. Chem. Soc.* **2016**, *138*, 15829−15832.

(20) Kulbak, M.; Gupta, S.; Kedem, N.; Levine, I.; Bendikov, T.; Hodes, G.; Cahen, D. *J. Phys. Chem. Lett.* **2016**, *7*, 167−172.

(21) Wang, Q.; Zheng, X.; Deng, Y.; Zhao, J.; Chen, Z.; Huang, J. *Joule* **2017**, *1*, 371−382.

(22) Zhao, D.; Yu, Y.; Wang, C.; Liao, W.; Shrestha, N.; Grice, C. R.; Cimaroli, A. J.; Guan, L.; Ellingson, R. J.; Zhu, K.; et al. *Nat. Energy* **2017**, *2*, 17018.

(23) McMeekin, D. P.; Sadoughi, G.; Rehman, W.; Eperon, G. E.; Saliba, M.; Hörantner, M. T.; Haghighirad, A.; Sakai, N.; Korte, L.; Rech, B.; et al. *Science* **2016**, *351*, 151−155.

(24) Bush, K. A.; Palmstrom, A. F.; Zhengshan, J. Y.; Boccard, M.; Cheacharoen, R.; Mailoa, J. P.; McMeekin, D. P.; Hoye, R. L.; Bailie, C. D.; Leijtens, T.; et al. *Nat. Energy* **2017**, *2*, 17009.

(25) Eperon, G. E.; Leijtens, T.; Bush, K. A.; Prasanna, R.; Green, T.; Wang, J. T.-W.; McMeekin, D. P.; Volonakis, G.; Milot, R. L.; May, R.; et al. *Science* **2016**, *354*, 861−865.

(26) Ahmad, W.; Khan, J.; Niu, G.; Tang, J. *Solar RRL* **2017**, *1*, 1700048.

(27) Wang, Y.; Zhang, T.; Kan, M.; Zhao, Y. *J. Am. Chem. Soc.* **2018**, *140*, 12345−12348.

(28) Wang, P.; Zhang, X.; Zhou, Y.; Jiang, Q.; Ye, Q.; Chu, Z.; Li, X.; Yang, X.; Yin, Z.; You, J. *Nat. Commun.* **2018**, *9*, 2225.

(29) Stoumpos, C. C.; Malliakas, C. D.; Kanatzidis, M. G. *Inorg. Chem.* **2013**, *52*, 9019−9038.

(30) Akkerman, Q. A.; Gandini, M.; Di Stasio, F.; Rastogi, P.; Palazon, F.; Bertoni, G.; Ball, J. M.; Prato, M.; Petrozza, A.; Manna, L. *Nat. Energy* **2017**, *2*, 16194.

(31) Chen, W.; Zhang, J.; Xu, G.; Xue, R.; Li, Y.; Zhou, Y.; Hou, J.; Li, Y. *Adv. Mater.* **2018**, *30*, 1800855.

(32) Lau, C. F. J.; Deng, X.; Ma, Q.; Zheng, J.; Yun, J. S.; Green, M. A.; Huang, S.; Ho-Baillie, A. W. *ACS Energy Lett.* **2016**, *1*, 573−577.

(33) Zeng, Q.; Zhang, X.; Feng, X.; Lu, S.; Chen, Z.; Yong, X.; Redfern, S. A.; Wei, H.; Wang, H.; Shen, H.; et al. *Adv. Mater.* **2018**, *30*, 1705393.

(34) Zhang, J.; Bai, D.; Jin, Z.; Bian, H.; Wang, K.; Sun, J.; Wang, Q.; Liu, S. *Adv. Energy Mater.* **2018**, *8*, 1703246.

(35) Sutton, R.; Eperon, G.; Miranda, L.; Parrott, E.; Kamino, B.; Patel, J.; Hörantner, M.; Johnston, M.; Haghighirad, A.; Moore, D.; et al. *Adv. Energy Mater.* **2016**, *6*, 1502458.

(36) Chen, C. Y.; Lin, H. Y.; Chiang, K. M.; Tsai, W. L.; Huang, Y. C.; Tsao, C. S.; Lin, H. W. *Adv. Mater.* **2017**, *29*, 1605290.

(37) Weissbuch, I.; Lahav, M.; Leiserowitz, L. *Cryst. Growth Des.* **2003**, *3*, 125.

(38) Chung, S.-Y.; Kim, Y.-M.; Kim, J.-G.; Kim, Y.-J. *Nat. Phys.* **2009**, *5*, 68.

(39) Burschka, J.; Pellet, N.; Moon, S.-J.; Humphry-Baker, R.; Gao, P.; Nazeeruddin, M. K.; Grätzel, M. *Nature* **2013**, *499*, 316.

(40) Liang, P. W.; Chueh, C. C.; Xin, X. K.; Zuo, F.; Williams, S. T.; Liao, C. Y.; Jen, A. K. Y. *Adv. Energy Mater.* **2015**, *5*, 1400960.

(41) Zhao, Y.; Wei, J.; Li, H.; Yan, Y.; Zhou, W.; Yu, D.; Zhao, Q. *Nat. Commun.* **2016**, *7*, 10228.

(42) Wang, Z.-K.; Gong, X.; Li, M.; Hu, Y.; Wang, J.-M.; Ma, H.; Liao, L.-S. *ACS Nano* **2016**, *10*, 5479−5489.

(43) Jiang, L. L.; Wang, Z. K.; Li, M.; Zhang, C. C.; Ye, Q. Q.; Hu, K. H.; Lu, D. Z.; Fang, P. F.; Liao, L. S. *Adv. Funct. Mater.* **2018**, *28*, 1705875.

(44) Yamashita, Y. *Sci. Technol. Adv. Mater.* **2009**, *10*, No. 024313.

(45) Nam, J. K.; Chai, S. U.; Cha, W.; Choi, Y. J.; Kim, W.; Jung, M. S.; Kwon, J.; Kim, D.; Park, J. H. *Nano Lett.* **2017**, *17*, 2028−2033.

(46) Appukkuttan, P.; Dehaen, W.; Fokin, V. V.; Van der Eycken, E. *Org. Lett.* **2004**, *6*, 4223−4225.

(47) Baradarani, M. M.; Farshi, H.; Khodaie, M.; Fazlelahi, H. Z.; Rashidi, A.; Joule, J. A. *J. Hetero. Chem.* **2018**, *55*, 91.

(48) Zeng, Z.; Zhang, J.; Gan, X.; Sun, H.; Shang, M.; Hou, D.; Lu, C.; Chen, R.; Zhu, Y.; Han, L. *Adv. Energy Mater.* **2018**, *8*, 1801050.

(49) Zeng, Q.; Zhang, X.; Feng, X.; Lu, S.; Chen, Z.; Yong, X.; Zhang, W.; et al. *Adv. Mater.* **2018**, *30*, 1705393.

(50) Lau, C. F. J.; Zhang, M.; Deng, X.; Zheng, J.; Bing, J.; Ma, Q.; Kim, J.; Hu, L.; Green, M. A.; Huang, S.; et al. *ACS Energy Lett.* **2017**, *2*, 2319−2325.

(51) Xu, W.; Zheng, L.; Zhang, X.; Cao, Y.; Meng, T.; Wu, D.; Liu, L.; Hu, W.; Gong, X. *Adv. Energy Mater.* **2018**, *8*, 1703178.

(52) Jahandar, M.; Heo, J. H.; Song, C. E.; Kong, K.-J.; Shin, W. S.; Lee, J.-C.; Im, S. H.; Moon, S.-J. *Nano Energy* **2016**, *27*, 330−339.

(53) Wang, H. Y.; Hao, M. Y.; Han, J.; Yu, M.; Qin, Y.; Zhang, P.; Guo, Z. X.; Ai, X. C.; Zhang, J. P. *Chem. - Eur. J.* **2017**, *23*, 3986−3992.

(54) Liu, F.; Dong, Q.; Wong, M. K.; Djurišić, A. B.; Ng, A.; Ren, Z.; Shen, Q.; Surya, C.; Chan, W. K.; Wang, J.; et al. *Proc. SPIE* **2016**, *6*, 1502206.

(55) Arunkumar, P.; Gil, K. H.; Won, S.; Unithrattil, S.; Kim, Y. H.; Kim, H. J.; Im, W. B. *J. Phys. Chem. Lett.* **2017**, *8*, 4161−4166.

(56) De, A.; Mondal, N.; Samanta, A. *Nanoscale* **2017**, *9*, 16722−16727.

(57) Wu, Z.; Bai, S.; Xiang, J.; Yuan, Z.; Yang, Y.; Cui, W.; Gao, X.; Liu, Z.; Jin, Y.; Sun, B. *Nanoscale* **2014**, *6*, 10505−10510.

(58) Feng, S.; Yang, Y.; Li, M.; Wang, J.; Cheng, Z.; Li, J.; Ji, G.; Yin, G.; Song, F.; Wang, Z.; Li, J.; Gao, X. *ACS Appl. Mater. Interfaces* **2016**, *8*, 14503−14512.

(59) Grancini, G.; Marras, S.; Prato, M.; Giannini, C.; Quarti, C.; De Angelis, F.; De Bastiani, M.; Eperon, G. E.; Snaith, H. J.; Manna, L.; Petrozza, A. *J. Phys. Chem. Lett.* **2014**, *5*, 3836−3842.

(60) Yang, Y.; Feng, S.; Xu, W.; Li, M.; Li, L.; Zhang, X.; Ji, G.; Zhang, X.; Wang, Z.; Xiong, Y.; Cao, L.; Sun, B.; Gao, X. *ACS Appl. Mater. Interfaces* **2017**, *9*, 23141−23151.

(61) Yang, Y.; Feng, S.; Li, M.; Li, F.; Zhang, C.; Han, Y.; Li, L.; Yuan, J.; Cao, L.; Wang, Z.; Sun, B.; Gao, X. *Nano Energy* **2018**, *48*, 10−19.

(62) Liao, P.; Zhao, X.; Li, G.; Shen, Y.; Wang, M.; et al. *Nano-Micro Lett.* **2018**, *10*, 5.

(63) Kim, J.; Yun, J.-H.; Kim, H.; Cho, Y.; Park, H.-H.; Kumar, M. M. D.; Yi, J.; Anderson, W. A.; Kim, D.-W. *Sci. Rep.* **2015**, *5*, 9256.

(64) Shao, Y.; Xiao, Z.; Bi, C.; Yuan, Y.; Huang, J. *Nat. Commun.* **2014**, *5*, 5784.

(65) Ruppel, W. *Helv. Phys. Acta* **1958**, *31*, 311−313.

(66) Lou, Y.; Xu, M.; Zhang, L.; Wang, Z.; Naka, S.; Okada, L.; Liao, L. *Org. Electron.* **2013**, *14*, 2698−2704.

(67) Adinolfi, V.; Yuan, M.; Comin, R.; Thibau, E.; Shi, D.; Saidaminov, M.; Kanjanaboos, P.; Kopilovic, D.; Hoogland, S.; Lu, Z.; et al. *Adv. Mater.* **2016**, *28*, 3406−3410.

(68) Li, M.; Wang, Z.; Yang, Y.; Hu, Y.; Feng, S.; Wang, J.; Gao, X.; Liao, L. *Adv. Mater.* **2016**, *6*, 1601156.

(69) Saidaminov, M.; Haque, M.; Almutlaq, J.; Sarmah, S.; Miao, X.; Begum, R.; Zhumekenov, A.; Dursun, I.; Cho, N.; Murali, B. *Adv. Mater.* **2017**, *5*, 1600704.